Bayesian Operational Modal Analysis with Asynchronous Data, Part II: Posterior Uncertainty

Yi-Chen Zhu[1] and Siu-Kui Au[2]

Institute for Risk and Uncertainty and Centre for Engineering Dynamics

University of Liverpool, United Kingdom

Abstract

A Bayesian modal identification method has been proposed in the companion paper that allows the most probable values of modal parameters to be determined using asynchronous ambient vibration data. This paper investigates the identification uncertainty of modal parameters in terms of their posterior covariance matrix. Computational issues are addressed. Analytical expressions are derived to allow the posterior covariance matrix to be evaluated accurately and efficiently. Synthetic, laboratory and field data examples are presented to verify the consistency, investigate potential modelling error and demonstrate practical applications.

Key Words: Asynchronous data, Bayesian methods, FFT, Field test, Operational modal analysis, Posterior uncertainty

1. Introduction

The identification uncertainty of modal parameters (e.g. natural frequencies, damping ratios and mode shapes) provides important information for risk assessment and structural health monitoring [1,2]. In operational modal analysis (OMA), the loading information is unknown and its intensity and frequency characteristics cannot be directly controlled. The identification uncertainty is often significantly larger than those in known input modal tests (like forced vibration or free vibration tests). Quantifying and Managing the uncertainty of identified modal parameters then becomes important for OMA.

[1] Corresponding author. Harrison Hughes Building, Brownlow Hill, Liverpool, L69 3GH, UK. Email: sgyzhu7@liverpool.ac.uk.
[2] Email: siukuiau@liverpool.ac.uk

For non-Bayesian or 'frequentist' methods, identification uncertainty is often assessed in terms of the ensemble variance of estimates over repeated experiments. Some challenges are discussed in [3]. For stochastic subspace idenfication (SSI), computational methods have been developed based on first-order perturbation for single setup data [4,5] and multi-setup data [6]. See also [7] for the variance of maximum likelihood modal parameter estimator in the state-space time domain. In a Bayesian context [8], identification uncertainty is quantified in terms of the covariance matrix associated with the 'posterior' (i.e. given data) distribution of modal parameters. For globally identifiable problems where the distribution has a single peak, the 'posterior covariance matrix' can be approximated by the inverse of Hessian of the negative log-likelihood function (NLLF) [9]. For OMA with synchronous data, efficient methods have been developed in different settings, e.g., well-separated modes [10], close modes [11] and multiple setups [12]. Mathematical connection between Bayesian and frequentist quantification of identification uncertainty has also been discussed [13]. Analytical expressions for the posterior covariance matrix have been derived under asymptotic conditions of long data and small damping, revealing the achievable identification precision of OMA [14]. See also [15] for work on related objectives but approached from a frequentist perspective for free vibration data.

A fast Bayesian OMA formulation for asynchronous data has been proposed in the companion paper; and an efficient method for determining the most probable values (MPV) of modal parameters has been developed. This paper investigates the posterior uncertainty of modal parameters and its efficient computation. Synthetic and laboratory data examples are presented to illustrate and verify the proposed OMA method. A field data example is also presented to illustrate real applications.

This paper is organized as follow. In Section 2, the NLLF for asynchronous data developed in the companion paper is briefly reviewed. In Section 3, computational issues associated with the posterior covariance matrix are discussed. Analytical expressions for the Hessian of NLLF (whose inverse gives the covariance matrix) are derived to allow accurate and efficient computation. The procedure for calculating the posterior covariance matrix is also summarised. In Section 4, synthetic, laboratory and field test examples are presented to illustrate the proposed method. Computational time is addressed in Section 5. Some comments regarding the practical issues are discussed in Section 6. The paper is concluded in Section 7.

2. NLLF for Asynchronous OMA Data

The posterior covariance matrix of modal parameters can be obtained as the inverse of the Hessian of negative log-likelihood function (NLLF). Consider the case of a well-separate mode where only one mode is dominant in the selected frequency band. Assume zero coherence among data of different synchronous data groups, it is shown in the companion paper that the NLLF is given by

$$L = \sum_{i=1}^{n_g} L_i \tag{1}$$

where

$$L_i = (n_i - 1)N_f \ln S_{ei} + \sum_k \ln(SD_k c_i + S_{ei}) + S_{ei}^{-1}\left(d_i - \bar{\mathbf{u}}_i^T \mathbf{A}_i \bar{\mathbf{u}}_i\right) \tag{2}$$

$$D_k = \left[\left(\beta_k^2 - 1\right)^2 + (2\zeta\beta_k)^2\right]^{-1} \qquad \beta_k = f/\mathrm{f}_k \tag{3}$$

$$d_i = \sum_k \mathcal{F}_{ik}^{\ *} \mathcal{F}_{ik} \tag{4}$$

$$\mathbf{A}_i = \sum_k \left(1 + S_{ei}/SD_k c_i\right)^{-1} \mathbf{D}_{ik} \tag{5}$$

$$\mathbf{D}_{ik} = \mathcal{F}_{ik} \mathcal{F}_{ik}^{\ *} \tag{6}$$

In the above equations, $\mathcal{F}_{ik}$ is the FFT of measured data associated with the i th synchronous group corresponding to frequency f_k in the selected frequency band; N_f is the number of FFT data in the band; f and ζ denote the natural frequency and damping ratio of the mode, respectively; $\mathbf{u}_i \in R^{n_i}$ is the mode shape measured by the i th group with n_i degrees of freedom (DOF) ; n_g is the total number of synchronous data groups; $c_i = \|\mathbf{u}_i\|^2$ and $\bar{\mathbf{u}}_i = \mathbf{u}_i / \|\mathbf{u}_i\|$ so that $\|\bar{\mathbf{u}}_i\| = 1$; S is the modal force PSD (power spectral density) and S_{ei} is the prediction error PSD of the i th group.

3. Posterior Uncertainty

The Hessian matrix of NLLF is a symmetric matrix containing the second derivatives of L with respect to (w.r.t.) $\boldsymbol{\theta} = \left\{f, \zeta, S, \{S_{ei}\}_{i=1}^{n_g}, \boldsymbol{\varphi}\right\}$. These derivatives will be derived analytically

in this section, allowing an accurate and efficient determination of Hessian without resorting to finite difference method.

The function L_i in Eq.(2) is first written explicitly in terms of the global mode shape $\boldsymbol{\varphi}$ to facilitate differentiation. Let $\mathbf{L}_i \in R^{n_i \times n}$ be a selection matrix so that $\mathbf{L}_i\boldsymbol{\varphi}$ gives the local mode shape confined to the DOFs in the ith group. The (j,k)-entry of $\mathbf{L}_i$ is equal to 1 if DOF k is measured by the jth channel in the ith synchronous group, and zero otherwise. Then c_i and $\bar{\mathbf{u}}_i$ can be expressed in terms of $\boldsymbol{\varphi}$:

$$c_i = \|\mathbf{L}_i\boldsymbol{\varphi}\|^2 = \boldsymbol{\varphi}^T\mathbf{L}_i^T\mathbf{L}_i\boldsymbol{\varphi} \tag{7}$$

$$\bar{\mathbf{u}}_i = \frac{\mathbf{L}_i\boldsymbol{\varphi}}{\|\mathbf{L}_i\boldsymbol{\varphi}\|} = \left(\boldsymbol{\varphi}^T\mathbf{L}_i^T\mathbf{L}_i\boldsymbol{\varphi}\right)^{-1/2}\mathbf{L}_i\boldsymbol{\varphi} \tag{8}$$

The global mode shape is subjected to unit norm constraint, i.e.,

$$\|\boldsymbol{\varphi}\|^2 = \boldsymbol{\varphi}^T\boldsymbol{\varphi} = 1 \tag{9}$$

This needs to be accounted for when evaluating Hessian to give posterior covariance matrix. One conventional way is to replace $\boldsymbol{\varphi}$ in the NLLF by its normalised counterpart

$$\bar{\boldsymbol{\varphi}} = \|\boldsymbol{\varphi}\|^{-1}\boldsymbol{\varphi} \tag{10}$$

so that the NLLF can be differentiated w.r.t. the free parameter $\boldsymbol{\varphi}$ without any constraints. Substituting Eq. (7) and (8) into the NLLF in Eq.(1) and replacing $\boldsymbol{\varphi}$ by $\|\boldsymbol{\varphi}\|^{-1}\boldsymbol{\varphi}$ gives:

$$L = \sum_{i=1}^{n_g}(n_i - 1)N_f \ln S_{ei} + \sum_{i=1}^{n_g}\sum_k \ln\left(SD_k \frac{\|\mathbf{L}_i\boldsymbol{\varphi}\|^2}{\boldsymbol{\varphi}^T\boldsymbol{\varphi}} + S_{ei}\right) + \sum_{i=1}^{n_g} S_{ei}^{-1}d_i - \frac{\boldsymbol{\varphi}^T\mathbf{A}'\boldsymbol{\varphi}}{\boldsymbol{\varphi}^T\boldsymbol{\varphi}} \tag{11}$$

where

$$\mathbf{A}' = \sum_{i=1}^{n_g} S_{ei}^{-1}\sum_k \left(\frac{\|\mathbf{L}_i\boldsymbol{\varphi}\|^2}{\boldsymbol{\varphi}^T\boldsymbol{\varphi}} + \frac{S_{ei}}{SD_k}\right)^{-1}\mathbf{L}_i^T\mathbf{D}_{ik}\mathbf{L}_i \tag{12}$$

The NLLF in Eq.(11) now is invariant to the scaling of $\boldsymbol{\varphi}$. Its Hessian at MPV is singular along the direction of $\boldsymbol{\varphi}$ [10]. This singularity is immaterial to posterior uncertainty because mode shape uncertainty is by definition orthogonal to such direction. The posterior covariance matrix is the 'pseudo-inverse' of the Hessian, i.e., via eigenvector representation

ignoring the singular component. Let $\{\lambda_i\}_{i=1}^{n_\theta}$ and $\{\mathbf{w}_i \in R^{n_\theta}\}_{i=1}^{n_\theta}$ be respectively the eigenvalues (in ascending order) and eigenvectors of the Hessian of the NLLF at MPV, where $n_\theta = n + n_g + 3$ is the number of modal parameters. Then $\lambda_1 = 0$ (singularity due to norm constraint) and

$$\mathbf{H}_L = \sum_{i=2}^{n_\theta} \lambda_i \mathbf{w}_i \mathbf{w}_i^T \tag{13}$$

The posterior covariance matrix is given by

$$\mathbf{C} = \sum_{i=2}^{n_\theta} \lambda_i^{-1} \mathbf{w}_i \mathbf{w}_i^T \tag{14}$$

3.1 Derivatives of NLLF

Analytical expressions for the derivatives of NLLF have been obtained by direct differentiation of Eq.(11). To facilitate analysis, the NLLF is first rewritten in terms of a_{ik}, b_{ik} and p_{ik}:

$$L = \sum_{i=1}^{n_g} (n_i - 1) N_f \ln S_{ei} + \sum_{i=1}^{n_g} \sum_k \ln b_{ik} + \sum_{i=1}^{n_g} S_{ei}^{-1} \left(d_{ik} - \sum_k a_{ik} p_{ik} \right) \tag{15}$$

where

$$a_{ik} = \left(\frac{\|\mathbf{L}_i \boldsymbol{\varphi}\|^2}{\boldsymbol{\varphi}^T \boldsymbol{\varphi}} + \frac{S_{ei}}{SD_k} \right)^{-1} \tag{16}$$

$$b_{ik} = SD_k \frac{\|\mathbf{L}_i \boldsymbol{\varphi}\|^2}{\boldsymbol{\varphi}^T \boldsymbol{\varphi}} + S_{ei} \tag{17}$$

$$p_{ik} = \frac{\boldsymbol{\varphi}^T \mathbf{L}_i^T \mathbf{D}_{ik} \mathbf{L}_i \boldsymbol{\varphi}}{\boldsymbol{\varphi}^T \boldsymbol{\varphi}} \tag{18}$$

appear frequently and their derivatives will be presented later in Section 3.2 to 3.4. In the following, a superscripted symbol denote the derivative w.r.t. that variable.

Auto-derivatives

$$L^{(ff)} = \sum_{i=1}^{n_g} \sum_k \left(\ln b_{ik}\right)^{(ff)} - \sum_{i=1}^{n_g} S_{ei}^{-1} \left(\sum_k a_{ik}^{(ff)} p_{ik} \right) \tag{19}$$

(similar expression for $L^{(\zeta\zeta)}$ and $L^{(SS)}$)

$$\begin{aligned} L^{(S_{ei}S_{ei})} = & -S_{ei}^{-2} N_f \left(n_i - 1\right) + \sum_k \left(\ln b_{ik}\right)^{(S_{ei}S_{ei})} - S_{ei}^{-1} \sum_k a_{ik}^{(S_{ei}S_{ei})} p_{ik} \\ & + 2S_{ei}^{-2} \sum_k a_{ik}^{(S_{ei})} p_{ik} + 2S_{ei}^{-3} \left(d_{ik} - \sum_k a_{ik} p_{ik} \right) \end{aligned} \tag{20}$$

$$\begin{aligned} L^{(\varphi\varphi)} = & \sum_{i=1}^{n_g} \sum_k \left(\ln b_{ik}\right)^{(\varphi\varphi)} - \sum_{i=1}^{n_g} S_{ei}^{-1} \sum_k a_{ik}^{(\varphi\varphi)} p_{ik} - \sum_{i=1}^{n_g} S_{ei}^{-1} \sum_k \left(a_{ik}^{(\varphi)}\right)^T p_{ik}^{(\varphi)} \\ & - \sum_{i=1}^{n_g} S_{ei}^{-1} \sum_k \left(p_{ik}^{(\varphi)}\right)^T a_{ik}^{(\varphi)} - \sum_{i=1}^{n_g} S_{ei}^{-1} \sum_k a_{ik} p_{ik}^{(\varphi\varphi)} \end{aligned} \tag{21}$$

Cross derivative

$$L^{(f\zeta)} = \sum_{i=1}^{n_g} \sum_k \left(\ln b_{ik}\right)^{(f\zeta)} - \sum_{i=1}^{n_g} S_{ei}^{-1} \left(\sum_k a_{ik}^{(f\zeta)} p_{ik} \right) \tag{22}$$

(similar expressions for $L^{(fS)}$ and $L^{(\zeta S)}$)

$$L^{(fS_{ei})} = \sum_k \left(\ln b_{ik}\right)^{(fS_{ei})} - S_{ei}^{-1} \sum_k a_{ik}^{(fS_{ei})} p_{ik} + S_{ei}^{-2} \sum_k a_{ik}^{(f)} p_{ik} \tag{23}$$

(similar expressions for $L^{(\zeta S_{ei})}$ and $L^{(SS_{ei})}$)

$$L^{(f\varphi)} = \sum_{i=1}^{n_g} \sum_k \left(\ln b_{ik}\right)^{(f\varphi)} - \sum_{i=1}^{n_g} S_{ei}^{-1} \sum_k a_{ik}^{(f\varphi)} p_{ik} - \sum_{i=1}^{n_g} S_{ei}^{-1} \sum_k a_{ik}^{(f)} p_{ik}^{(\varphi)} \tag{24}$$

(similar expressions for $L^{(\zeta\varphi)}$ and $L^{(S\varphi)}$)

$$L^{(S_{ei}\varphi)} = \sum_k \left(\ln b_{ik}\right)^{(S_{ei}\varphi)} - S_{ei}^{-1} \left(\sum_k a_{ik}^{(S_{ei}\varphi)} p_{ik} + \sum_k a_{ik}^{(S_{ei})} p_{ik}^{(\varphi)} \right) + S_{ei}^{-2} \left(\sum_k a_{ik}^{(\varphi)} p_{ik} + \sum_k a_{ik} p_{ik}^{(\varphi)} \right) \tag{25}$$

3.2 Derivatives of a_{ik}

Note that a_{ik} is in the form of x^{-1}. It is easier to evaluate the derivatives of its reciprocal a_{ik}^{-1}.

For any two parameters x_1 and x_2 in $\{f, \zeta, S, \{S_{ei}\}, \boldsymbol{\varphi}\}$,

$$a_{ik}^{(x_1)} = -a_{ik}^2 \left(a_{ik}^{-1}\right)^{(x_1)} \tag{26}$$

and

$$a_{ik}^{(x_1x_2)} = 2a_{ik}^3 \left(a_{ik}^{-1}\right)^{(x_1)} \left(a_{ik}^{-1}\right)^{(x_2)} - a_{ik}^2 \left(a_{ik}^{-1}\right)^{(x_1x_2)} \tag{27}$$

In Eq.(27), when x_1 and x_2 are both equal to $\boldsymbol{\varphi}$, the second derivative of a_{ik} with respect to $\boldsymbol{\varphi}$ is given by

$$a_{ik}^{(\boldsymbol{\varphi}\boldsymbol{\varphi})} = 2a_{ik}^3 \left[\left(a_{ik}^{-1}\right)^{(\boldsymbol{\varphi})}\right]^T \left(a_{ik}^{-1}\right)^{(\boldsymbol{\varphi})} - a_{ik}^2 \left(a_{ik}^{-1}\right)^{(\boldsymbol{\varphi}\boldsymbol{\varphi})} \tag{28}$$

It remains to determine the first and second derivatives of a_{ik}^{-1}, which are given in Table 1 and Table 2, respectively. The expressions involve the derivatives of D_k, which are given in the Appendix.

Table 1. First Derivatives of a_{ik}^{-1}

$x =$	f, ζ	S	S_{ei}	$\boldsymbol{\varphi}$
$\left(a_{ik}^{-1}\right)^{(x)}$	$\frac{S_{ei}}{S}\left(D_k^{-1}\right)^{(x)}$	$-\frac{S_{ei}}{S^2 D_k}$	$\frac{1}{SD_k}$	$\frac{2\boldsymbol{\varphi}^T \mathbf{L}_i^T \mathbf{L}_i}{\boldsymbol{\varphi}^T\boldsymbol{\varphi}} - \frac{2\boldsymbol{\varphi}^T \left\|\mathbf{L}_i\boldsymbol{\varphi}\right\|^2}{\left(\boldsymbol{\varphi}^T\boldsymbol{\varphi}\right)^2}$

Table 2. Second Derivatives of a_{ik}^{-1}

$\left(a_{ik}^{-1}\right)^{(xy)}$ $y =$	f, ζ	S	S_{ei}	$\boldsymbol{\varphi}$
$x =$				
f, ζ	$\frac{S_{ei}}{S}\left(D_k^{-1}\right)^{(xy)}$	$-\frac{S_{ei}}{S^2}\left(D_k^{-1}\right)^{(x)}$	$\frac{1}{S}\left(D_k^{-1}\right)^{(x)}$	$\mathbf{0}$
S		$\frac{2S_{ei}}{S^3 D_k}$	$-\frac{1}{S^2 D_k}$	$\mathbf{0}$
S_{ei}	sym.		0	$\mathbf{0}$
$\boldsymbol{\varphi}$				See note

Note: $\left(a_{ik}^{-1}\right)^{(\boldsymbol{\varphi}\boldsymbol{\varphi})} = \frac{2\mathbf{L}_i^T\mathbf{L}_i}{\boldsymbol{\varphi}^T\boldsymbol{\varphi}} - \frac{4\boldsymbol{\varphi}\boldsymbol{\varphi}^T\mathbf{L}_i^T\mathbf{L}_i}{\left(\boldsymbol{\varphi}^T\boldsymbol{\varphi}\right)^2} + \frac{8\boldsymbol{\varphi}\boldsymbol{\varphi}^T\left\|\mathbf{L}_i\boldsymbol{\varphi}\right\|^2}{\left(\boldsymbol{\varphi}^T\boldsymbol{\varphi}\right)^3} - \frac{4\mathbf{L}_i^T\mathbf{L}_i\boldsymbol{\varphi}\boldsymbol{\varphi}^T}{\left(\boldsymbol{\varphi}^T\boldsymbol{\varphi}\right)^2} - \frac{2\left\|\mathbf{L}_i\boldsymbol{\varphi}\right\|^2}{\left(\boldsymbol{\varphi}^T\boldsymbol{\varphi}\right)^2}\mathbf{I}_n$.

3.3 Derivatives of $\ln b_{ik}$

The derivatives of $\ln b_{ik}$ can be expressed through those of b_{ik}, which is easier to derive. For any two parameters x_1 and x_2 in $\{f, \zeta, S, \{S_{ei}\}, \boldsymbol{\varphi}\}$,

$$\left(\ln b_{ik}\right)^{(x_1)} = \frac{1}{b_{ik}} b_{ik}^{(x_1)} \tag{29}$$

$$\left(\ln b_{ik}\right)^{(x_1 x_2)} = -\left(\frac{1}{b_{ik}}\right)^2 b_{ik}^{(x_1)} b_{ik}^{(x_2)} + \frac{1}{b_{ik}} b_{ik}^{(x_1 x_2)} \tag{30}$$

In Eq.(30), when x_1 and x_2 are both equal to $\boldsymbol{\varphi}$, the second derivative of $\ln b_{ik}$ with respect to $\boldsymbol{\varphi}$ is given by

$$\left(\ln b_{ik}\right)^{(\boldsymbol{\varphi}\boldsymbol{\varphi})} = -\left(\frac{1}{b_{ik}}\right)^2 \left(b_{ik}^{(\boldsymbol{\varphi})}\right)^T b_{ik}^{(\boldsymbol{\varphi})} + \frac{1}{b_{ik}} b_{ik}^{(\boldsymbol{\varphi}\boldsymbol{\varphi})} \tag{31}$$

It remains to determine the first and second derivatives of b_{ik}, which are given in Table 3 and Table 4, respectively.

Table 3. First Derivatives of b_{ik}

$x =$	f, ζ	S	S_{ei}	$\boldsymbol{\varphi}$
$b_{ik}^{(x)}$	$D_k^{(x)} \dfrac{\left\|\mathbf{L}_i\boldsymbol{\varphi}\right\|^2}{\boldsymbol{\varphi}^T\boldsymbol{\varphi}}$	$D_k \dfrac{\left\|\mathbf{L}_i\boldsymbol{\varphi}\right\|^2}{\boldsymbol{\varphi}^T\boldsymbol{\varphi}}$	1	$2SD_k\left(\dfrac{\boldsymbol{\varphi}^T\mathbf{L}_i^T\mathbf{L}_i}{\boldsymbol{\varphi}^T\boldsymbol{\varphi}} - \dfrac{\boldsymbol{\varphi}^T\left\|\mathbf{L}_i\boldsymbol{\varphi}\right\|^2}{\left(\boldsymbol{\varphi}^T\boldsymbol{\varphi}\right)^2}\right)$

Table 4. Second Derivatives of b_{ik}

$b_{ik}^{(xy)}$ $y =$	f, ζ	S	S_{ei}	$\boldsymbol{\varphi}$
$x =$				
f, ζ	$SD_k^{(xy)} \dfrac{\left\|\mathbf{L}_i\boldsymbol{\varphi}\right\|^2}{\boldsymbol{\varphi}^T\boldsymbol{\varphi}}$	$D_k^{(x)} \dfrac{\left\|\mathbf{L}_i\boldsymbol{\varphi}\right\|^2}{\boldsymbol{\varphi}^T\boldsymbol{\varphi}}$	0	$2SD_k^{(x)}\left(\dfrac{\boldsymbol{\varphi}^T\mathbf{L}_i^T\mathbf{L}_i}{\boldsymbol{\varphi}^T\boldsymbol{\varphi}} - \dfrac{\boldsymbol{\varphi}^T\left\|\mathbf{L}_i\boldsymbol{\varphi}\right\|^2}{\left(\boldsymbol{\varphi}^T\boldsymbol{\varphi}\right)^2}\right)$
S		0	0	$2D_k\left(\dfrac{\boldsymbol{\varphi}^T\mathbf{L}_i^T\mathbf{L}_i}{\boldsymbol{\varphi}^T\boldsymbol{\varphi}} - \dfrac{\boldsymbol{\varphi}^T\left\|\mathbf{L}_i\boldsymbol{\varphi}\right\|^2}{\left(\boldsymbol{\varphi}^T\boldsymbol{\varphi}\right)^2}\right)$
S_{ei}	sym.		0	$\mathbf{0}$
$\boldsymbol{\varphi}$				See note

Note: $b_{ik}^{(\boldsymbol{\varphi}\boldsymbol{\varphi})} = SD_k\left(\dfrac{2\mathbf{L}_i^T\mathbf{L}_i}{\boldsymbol{\varphi}^T\boldsymbol{\varphi}} - \dfrac{4\boldsymbol{\varphi}\boldsymbol{\varphi}^T\mathbf{L}_i^T\mathbf{L}_i}{\left(\boldsymbol{\varphi}^T\boldsymbol{\varphi}\right)^2} + \dfrac{8\boldsymbol{\varphi}\boldsymbol{\varphi}^T\left\|\mathbf{L}_i\boldsymbol{\varphi}\right\|^2}{\left(\boldsymbol{\varphi}^T\boldsymbol{\varphi}\right)^3} - \dfrac{4\mathbf{L}_i^T\mathbf{L}_i\boldsymbol{\varphi}\boldsymbol{\varphi}^T}{\left(\boldsymbol{\varphi}^T\boldsymbol{\varphi}\right)^2} - \dfrac{2\left\|\mathbf{L}_i\boldsymbol{\varphi}\right\|^2}{\left(\boldsymbol{\varphi}^T\boldsymbol{\varphi}\right)^2}\mathbf{I}_n\right)$.

3.4 Derivatives of p_{ik}

The first and second derivatives of p_{ik} w.r.t. the global mode shape $\boldsymbol{\varphi}$ are given by

$$p_{ik}^{(\boldsymbol{\varphi})} = \frac{2\boldsymbol{\varphi}^T \mathbf{L}_i^T \mathbf{D}_{ik} \mathbf{L}_i}{\boldsymbol{\varphi}^T \boldsymbol{\varphi}} - \frac{2\boldsymbol{\varphi}^T \mathbf{L}_i^T \mathbf{D}_{ik} \mathbf{L}_i \boldsymbol{\varphi} \boldsymbol{\varphi}^T}{\left(\boldsymbol{\varphi}^T \boldsymbol{\varphi}\right)^2} \tag{32}$$

$$\begin{aligned} p_{ik}^{(\boldsymbol{\varphi}\boldsymbol{\varphi})} = & \frac{2\mathbf{L}_i^T \mathbf{D}_{ik} \mathbf{L}_i}{\boldsymbol{\varphi}^T \boldsymbol{\varphi}} - \frac{4\boldsymbol{\varphi}\boldsymbol{\varphi}^T \mathbf{L}_i^T \mathbf{D}_{ik} \mathbf{L}_i}{\left(\boldsymbol{\varphi}^T \boldsymbol{\varphi}\right)^2} + \frac{8\boldsymbol{\varphi}\boldsymbol{\varphi}^T \left(\boldsymbol{\varphi}^T \mathbf{L}_i^T \mathbf{D}_{ik} \mathbf{L}_i \boldsymbol{\varphi}\right)}{\left(\boldsymbol{\varphi}^T \boldsymbol{\varphi}\right)^3} \\ & - \frac{4\mathbf{L}_i^T \mathbf{D}_{ik} \mathbf{L}_i \boldsymbol{\varphi}\boldsymbol{\varphi}^T}{\left(\boldsymbol{\varphi}^T \boldsymbol{\varphi}\right)^2} - \frac{2\boldsymbol{\varphi}^T \mathbf{L}_i^T \mathbf{D}_{ik} \mathbf{L}_i \boldsymbol{\varphi} \mathbf{I}_n}{\left(\boldsymbol{\varphi}^T \boldsymbol{\varphi}\right)^2} \end{aligned} \tag{33}$$

3.5 Dimensionless Scaling

The modal parameters have different units and hence different orders of magnitude and sensitivity in the NLLF. Different entries in the Hessian of NLLF will have large disparity in magnitude, which makes the matrix ill-conditioned when calculating inverse. One way to overcome this problem is to normalise the entries by the corresponding MPVs so that the resulting Hessian is dimensionless. Let $\boldsymbol{\theta} = [f; \zeta; S; S_{e1}; ...; S_{en_g}; \boldsymbol{\varphi}]$ denote the vector of modal parameters and $\hat{\boldsymbol{\theta}} = [\hat{f}; \hat{\zeta}; \hat{S}; \hat{S}_{e1}; ...; \hat{S}_{en_g}]$ denote the vector of MPVs except the global mode shape. Define the dimensionless vector

$$\mathbf{a} = \mathbf{T}\boldsymbol{\theta} \tag{34}$$

where

$$\mathbf{T} = \begin{bmatrix} diag\left(\hat{\boldsymbol{\theta}}\right)^{-1} & \\ & \mathbf{I}_n \end{bmatrix} \tag{35}$$

That is, except for the global mode shape (which is already scaled to unit norm), the remaining entries of $\mathbf{a}$ is the ratio of the modal parameters to the corresponding MPVs. The NLLF now can be expressed as $L\left(\mathbf{T}^{-1}\mathbf{a}\right)$ and the Hessian matrix w.r.t. $\mathbf{a}$ at MPV is given by

$$\mathbf{H}_L' = \mathbf{T}^{-T} \mathbf{H}_L \mathbf{T}^{-1} \tag{36}$$

which is dimensionless. The posterior covariance matrix of $\mathbf{a}$, i.e., pseudo-inverse of $\mathbf{H}_L'$, is also dimensionless. Its diagonal entry gives directly the square of coefficient of variation (c.o.v.) of the corresponding modal parameter.

3.6 Summary of Procedure

The procedure of determining the posterior covariance matrix of modal parameters is summarised as follow:

1. Calculate the entries of the Hessian matrix using the equations in Section 3.1 with the help of the equations in Section 3.2, 3.3 and 3.4.
2. Assemble the Hessian matrix and calculate the dimensionless one according to Eq.(36).
3. Perform eigenvector decomposition of the Hessian matrix and calculate the posterior covariance matrix according to Eq.(14).
4. The posterior c.o.v. can be directly obtained from the square root of the corresponding diagonal term of the posterior covariance matrix.
5. The posterior c.o.v. of the overall mode shape can be expressed as the square root sum of the eigenvalues of its covariance matrix, equal to the corresponding partition in the full posterior covariance matrix [16].

4. Illustrative Examples

Four examples are presented in this section to illustrate the proposed method and its practical applications. The first example investigates potential modelling error due to zero coherence approximation. The next two examples are continuations of Section 9.1 and 9.2 in the companion paper, respectively, but now the focus is on identification uncertainty. The last example applies the proposed method to a full-scale building. It illustrates the issues encountered in real applications with asynchronous data.

4.1 Effect of Zero Coherence Approximation

The proposed modal identification algorithm in this work assumes zero coherence between different synchronous groups so that efficient strategies can be developed. However, this assumption may not hold for real asynchronous data, causing potential modelling errors. Potential bias in the MPVs and posterior c.o.v.s is investigated in this section through a parametric study with synthetic data. Potential modelling error is investigated here by comparing Bayesian and frequentist statistics [13]. It has been reasoned mathematically, and demonstrated numerically and experimentally with laboratory and field data, that if there is no modelling error then the ensemble average of modal parameter MPV is approximately equal to the exact value that generated the synthetic data; and the ensemble mean of posterior

variance is approximately equal to the ensemble variance of MPV. In the general case, the discrepancy between the two sets of quantities indicates modelling error.

Consider a six-storey shear building structure with uniform inter-storey stiffness 3000kN/mm and floor mass 600 tons. The natural frequency of the first mode is calculated to be 2.71Hz. The damping ratios of all the modes are assumed to be 1%. The structure is subjected to independent and identically distributed (i.i.d.) Gaussian white noise excitation with a PSD of $11.8\text{N}/\sqrt{\text{Hz}}$ in the horizontal direction. The resulting acceleration response is in the order of few tens of $\mu\text{g}/\sqrt{\text{Hz}}$ around the resonance peak of a mode. Uniaxial accelerometers are distributed on each storey measuring the structural response in horizontal direction. The measured data comprises two synchronous groups measuring 1/F to 3/F (Group 1) and 4/F to 6/F (Group 2). To simulate imperfect synchronisation, the modal excitation between these two groups are correlated with a coherence of χ, which will be varied in the parametric study. This was done by generating two independent modal excitations (say p_1 and p_2), using p_1 as the modal excitation of Group 1 and $\chi p_1 + \sqrt{1-\chi^2}\, p_2$ as the modal excitation of Group 2. The measured acceleration data is contaminated by Gaussian white noise with PSDs $40\mu\text{g}^2/\text{Hz}$ and $90\mu\text{g}^2/\text{Hz}$ for Group 1 and 2, respectively.

Four scenarios with increasing coherence are considered, i.e. $\chi = 0$ (totally asynchronous, no modelling error), 0.2 (low coherence), 0.6 (high coherence) and 1 (perfectly synchronous). For each scenario, acceleration data is sampled at 100Hz for a duration of 500s.

Figure 1 shows the singular value spectrum of a typical set of data with a coherence of 0.2. The two lines associated with each resonance peak are indicative of two asynchronous groups. The horizontal bars '[-]' indicate the selected frequency bands for modal identification and the squares denote the initial guesses of the natural frequencies. The six modes indicated in the figure are identified separately using the FFT data within each selected frequency band.

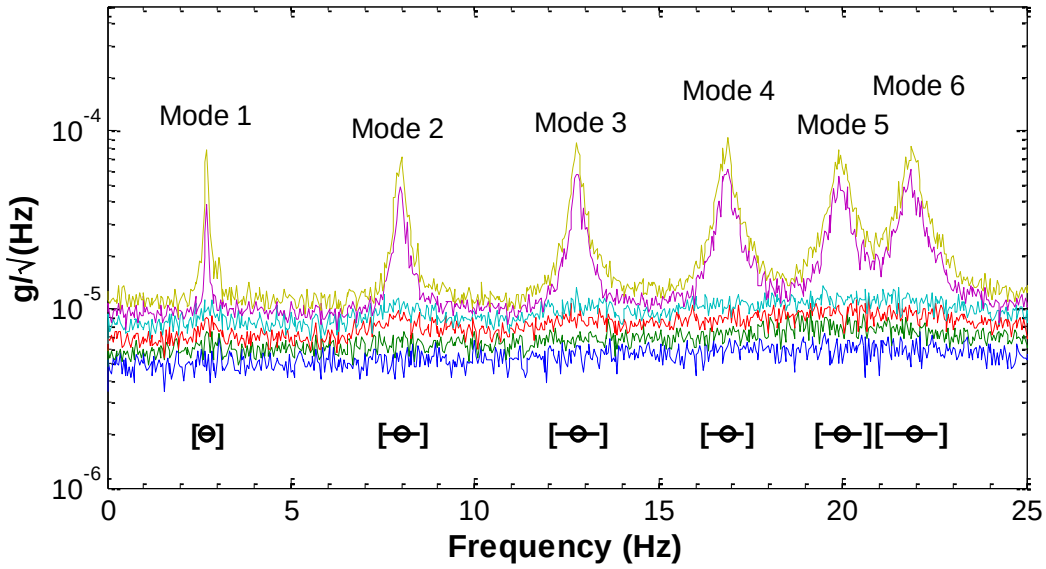

Figure 1. Root Singular Value Spetrum of a Typical Data Set, Coherence=0.2

Table 5. Sample and Bayesian Statistics, Coherence=0 (Perfectly Incoherent Data).

Mode		Exact (A)	Sample Mean (B)	A/B	Freq. (%) (C)	Bay. (%) (D)	C/D
$f(\text{Hz})$	1	2.713	2.713	1.00	0.09	0.10	0.98
	2	7.981	7.981	1.00	0.06	0.06	1.05
	3	12.786	12.786	1.00	0.04	0.04	0.95
	4	16.847	16.847	1.00	0.04	0.04	1.04
	5	19.930	19.931	1.00	0.04	0.04	0.99
	6	21.854	21.846	1.00	0.04	0.04	0.96
$\zeta(\%)$	1	1	1.02	0.98	11.55	11.20	1.03
	2	1	1.01	0.99	6.35	6.36	1.00
	3	1	1.01	0.99	5.44	5.38	1.01
	4	1	1.00	1.00	5.77	5.78	1.00
	5	1	1.02	0.98	5.64	5.48	1.03
	6	1	1.05	0.95	4.75	4.86	0.98

Table 6. Sample and Bayesian Statistics, Coherence=0.2 (Low Coherence Data).

Mode		Exact (A)	Sample Mean (B)	A/B	Freq. (%) (C)	Bay. (%) (D)	C/D
$f(\mathrm{Hz})$	1	2.713	2.713	1.00	0.10	0.10	1.02
	2	7.981	7.981	1.00	0.06	0.06	1.06
	3	12.786	12.786	1.00	0.04	0.04	1.00
	4	16.847	16.847	1.00	0.04	0.04	1.03
	5	19.930	19.931	1.00	0.04	0.04	1.05
	6	21.854	21.846	1.00	0.04	0.04	1.02
$\zeta(\%)$	1	1	1.02	0.98	11.62	11.20	1.04
	2	1	1.01	0.99	6.32	6.35	1.00
	3	1	1.00	1.00	5.59	5.38	1.04
	4	1	1.00	1.00	5.81	5.78	1.01
	5	1	1.03	0.97	5.78	5.48	1.05

Table 7. Sample and Bayesian Statistics, Coherence=0.6 (High Coherence Data).

Mode		Exact (A)	Sample Mean (B)	A/B	Freq. (%) (C)	Bay. (%) (D)	C/D
$f(\mathrm{Hz})$	1	2.713	2.713	1.00	0.11	0.10	1.16
	2	7.981	7.981	1.00	0.06	0.06	1.14
	3	12.786	12.786	1.00	0.05	0.04	1.09
	4	16.847	16.847	1.00	0.05	0.04	1.11
	5	19.930	19.932	1.00	0.05	0.04	1.13
	6	21.854	21.846	1.00	0.04	0.04	1.08
$\zeta(\%)$	1	1	1.02	0.98	13.02	11.20	1.16
	2	1	1.01	0.99	7.26	6.36	1.14
	3	1	1.00	1.00	6.20	5.38	1.15

	4	1	1.00	1.00	6.42	5.78	1.11
	5	1	1.03	0.97	6.12	5.48	1.12
	6	1	1.05	0.95	5.58	4.86	1.15

Table 8. Sample and Bayesian Statistics, Coherence=1 (Synchronous Data).

Mode		Exact (A)	Sample Mean (B)	A/B	Freq. (%) (C)	Bay. (%) (D)	C/D
$f(\mathrm{Hz})$	1	2.713	2.713	1.00	0.13	0.10	1.36
	2	7.981	7.982	1.00	0.08	0.06	1.38
	3	12.786	12.786	1.00	0.06	0.04	1.33
	4	16.847	16.846	1.00	0.06	0.04	1.36
	5	19.930	19.932	1.00	0.05	0.04	1.35
	6	21.854	21.846	1.00	0.05	0.04	1.33
$\zeta(\%)$	1	1	1.02	0.98	15.26	11.22	1.36
	2	1	1.01	0.99	8.47	6.36	1.33
	3	1	1.00	1.00	7.57	5.38	1.41
	4	1	1.01	0.99	8.04	5.78	1.39
	5	1	1.03	0.97	7.66	5.48	1.40
	6	1	1.05	0.95	6.47	4.86	1.33

Bias in MPV

Table 5 to Table 8 compare the frequentist and Bayesian statistics of modal identification results among 1000 i.i.d. data sets. The column ‘Exact’ shows the exact values that generated the data. The next column shows the sample mean of the MPV among the 1000 data sets. The ratio between these two values are shown in the column ‘A/B’. The ratios are all close to 1, suggesting little or practically no bias in the MPV of natural frequency and damping ratio.

Bias in identification uncertainty

The column ‘Freq.’ (short for ‘frequentist’) shows the sample c.o.v. of the MPV, i.e., the ratio of the sample standard deviation to the sample mean of MPV. The column ‘Bay.’ (short for

Bayesian) shows the sample root mean square value of the posterior standard deviation divided by the sample mean of the MPV. The column 'C/D' shows their ratio. As coherence increases, the ratio stays above 1 and deviates to a greater extent from 1, suggesting an increasing under-estimation of identification uncertainty due to modelling error of zero coherence assumption. Nevertheless, this bias is practically insignificant. For a high coherence of 60% (Table 7), the under-estimation is only 10%. In the extreme (unreasonable) case of 100% coherence (i.e., perfectly synchronised data, Table 8), it is 40%.

Mode shape

Table 9 to Table 12 compare the identification uncertainty of the mode shapes between the frequentist and Bayesian statistics. The frequentist uncertainty of the MPV of mode shape (column 'Freq.') is calculated based on the sample mean of MAC between the MPV of mode shape and the exact mode shape. The values in this column are all close to 1 (to five decimal places), suggesting little or practically no bias in the mode shape MPVs. The Bayesian uncertainty (column 'Bay.') is investigated based on the sample average of expected MAC, which can be calculated as:

$$\text{Expected MAC} = \left(1 + \text{mode shape c.o.v.}^2\right)^{-1/2} \tag{37}$$

where the mode shape c.o.v. is calculated as the square root sum of the eigenvalues of its covariance matrix. The column 'C/D' shows the ratio of frequentist to Bayesian uncertainty. The ratio is close to 1 for all cases of coherence, indicating practically no bias in mode shape uncertainty.

Table 9. Sample and Bayesian Statistics of Mode Shapes, Coherence=0

Mode	Freq. (C)	Bay. (D)	C/D
1	0.99943	0.99944	0.99999
2	0.99975	0.99977	0.99998
3	0.99976	0.99983	0.99994
4	0.99962	0.99982	0.99980
5	0.99947	0.99983	0.99964
6	0.99922	0.99986	0.99936

Table 10. Sample and Bayesian Statistics of Mode Shapes, Coherence=0.2

Mode	Freq. (C)	Bay. (D)	C/D
1	0.99946	0.99944	1.00003
2	0.99976	0.99977	0.99999
3	0.99977	0.99983	0.99994
4	0.99965	0.99982	0.99983
5	0.99946	0.99983	0.99963
6	0.99923	0.99986	0.99937

Table 11. Sample and Bayesian Statistics of Mode Shapes, Coherence=0.6

Mode	Freq. (C)	Bay. (D)	C/D
1	0.99953	0.99944	1.00010
2	0.99979	0.99977	1.00002
3	0.99980	0.99983	0.99997
4	0.99969	0.99982	0.99987
5	0.99949	0.99983	0.99966
6	0.99928	0.99986	0.99942

Table 12. Sample and Bayesian Statistics of Mode Shapes, Coherence=1

Mode	Freq. (C)	Bay. (D)	C/D
1	0.99973	0.99944	1.00029
2	0.99989	0.99977	1.00012
3	0.99993	0.99983	1.00010
4	0.99993	0.99982	1.00012
5	0.99990	0.99983	1.00007
6	0.99976	0.99986	0.99991

The number of data sets (1000) used here is large enough so that statistical estimation error is negligible. Repeated runs have also been conducted, which shows qualitatively the same results as those presented here. Based on the evidence provided, it is fair to say that the

modelling error of zero coherence assumption does not cause significant bias in the posterior MPV. There is an under-estimation in identification uncertainty of natural frequency and damping ratio. Nevertheless, it is not significant unless the coherence among different synchronous groups is extremely close to one (e.g. >0.99), where the data channels can be considered as practically synchronised in real applications. In the latter case, it is more appropriate to identify the modes using a conventional algorithm that assumes synchronous data.

4.2 Synthetic Data Example

Recall the example in Section 9.1 of the companion paper, where the synthetic data of 1000s duration consists of six channels measuring the horizontal acceleration of different floors (1-2/F by Group 1; 3-4/F by Group 2; 5-6/F by Group 3). Table 13 shows the posterior c.o.v. of modal parameters using the proposed method. Consistent with common observations, the posterior c.o.v. of natural frequencies (range between 0.03% and 0.05%) is much smaller than those of damping ratios (range between 1.3% and 2.7%). The results agree with those calculated using finite difference method (details omitted here), verifying their correctness.

Table 13. Identified Modal Parameter c.o.v., Synthetic Data Example

Mode	f c.o.v. (%)	ζ c.o.v. (%)	$\sqrt{S}$ c.o.v. (%)	$\sqrt{S_{ej}}$ c.o.v. (%)	$\boldsymbol{\varphi}$ c.o.v. (%)
1	0.05	6.10	2.7	2.9 2.9 2.9	2.3
2	0.03	3.38	1.3	1.6 1.6 1.6	1.4
3	0.03	2.95	1.4	1.4 1.4 1.4	1.3
4	0.04	3.71	2.4	1.6 1.6 1.6	1.4

4.3 Laboratory Shear Building Example

Recall the example in Section 9.2 of the companion paper, where thirty-minute acceleration response of a four-storey laboratory shear frame in weak direction was recorded in both synchronous and asynchronous manner. The posterior c.o.v.s for the synchronous data set are obtained using the fast Bayesian FFT method [11] and the ones for the asynchronous data set are obtained using the proposed method. The results are shown in Table 14.

Table 14. Posterior Uncertainty (c.o.v.), Laboratory Shear Building

Mode	f c.o.v. (10^{-3})		ζ c.o.v. (%)		$\sqrt{S}$ c.o.v. (%)		$\sqrt{S_{ej}}$ c.o.v. (%)	
	Asyn.	Syn.	Asyn.	Syn.	Asyn.	Syn.	Asyn.	Syn.
1	0.13	0.17	21.5	29.3	10.4	12.7	8.10 8.22	4.74
2	0.11	0.16	9.91	13.3	5.11	6.67	3.71 3.70	2.15
3	0.04	0.06	10.9	15.4	3.55	4.47	3.71 3.70	2.15
4	0.08	0.11	6.65	7.78	2.83	3.89	2.63 2.63	1.52
5	0.11	0.16	7.08	9.66	4.21	5.60	2.61 2.62	1.52

Theoretically, the posterior c.o.v. of modal parameters for these two data sets cannot be directly compared as they are calculated based on different data. However, they should be practically the same as the data used for inference in these two sets is measured based on the same experimental condition, i.e., the same duration, excitation and noise environment. Intuitively, the posterior c.o.v. for asynchronous data tends to be higher than that of the synchronous one. This is not the case with the results in the table, however. For natural frequency, damping ratio and modal force PSD, the posterior c.o.v. calculated based on the asynchronous data set are generally less than the synchronous counterpart. This is attributed to the bias-low nature of the algorithm due to the zero coherence assumption. The bias in c.o.v. is in the order of 20% lower. Additional analysis reveals that the coherence among different channels is about 0.9, which is relatively high. The bias based on this coherence is

consistent with the findings of the parametric study in Section 4.1. Despite this apparently high value of coherence, the singular value spectrum (in Figure 5 of the companion paper) already exhibits artificial modes, and one will get erroneous modal identification results using an algorithm that assumes synchronous data.

The posterior uncertainty of the prediction error PSD calculated based on the asynchronous data set is larger than the one for the synchronous data set. This is because the prediction error PSD is only modelled to be the same within each synchronous group in the proposed method. For the synchronous counterpart, the prediction error PSD is modelled to be the same in all measured DOFs (hence intuitively more data for inference). However, it has higher modelling error risk because the prediction error PSD of different groups in reality need not be the same.

4.4 Brodie Tower

The proposed method is next applied to field data. The instrumented structure is the Brodie Tower (Figure 2) at the University of Liverpool, UK. It is an eight-storey reinforced concrete building. As shown in Figure 3, The ground floor of the building is connected to the Muspratt Building with a shape close to a rectangle. From the first floor to the seventh floor, the floors are T-shaped.

Figure 2. Overview of Brodie Tower

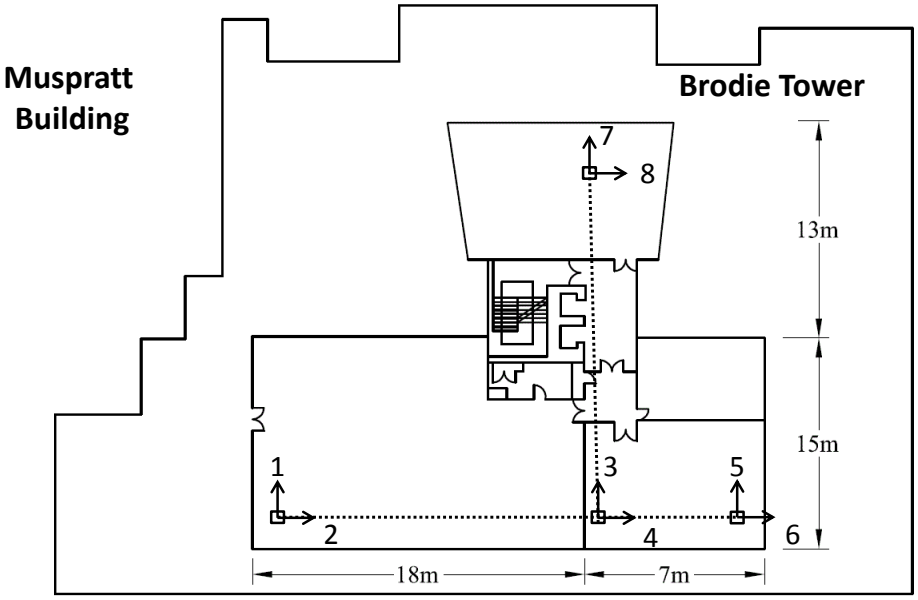

Figure 3. Plan View of Brodie Tower Building, Sixth Floor

Figure 4. Force-Balance Accelerometer on Site

Ambient data was measured on the sixth floor of the building. Four tri-axial force-balance accelerometers were used (see Figure 4). The test focused on the lateral mode of the whole building. Biaxial acceleration at four locations, i.e., $2 \times 4 = 8$ DOFs, are used for analysis. Figure 3 shows the plan view of the floor and the locations to be measured. The data was sampled at 50Hz with a duration of 20mins. Each sensor used its own clock for sampling and

so the sampled data between different sensors are not synchronised. Within the frequency range of interest, the measurement noise intensity is in the order of $0.5\mu g/\sqrt{Hz}$ as evidenced from the baseline level of the root singular value spectrum in Figure 5.

Figure 5 shows the root singular value spectrum of the measured data. The first six modes marked in the figure are investigated. The hand-picked initial guesses and the selected frequency bands are shown with circles and the symbol '[-]', respectively. The identified MPVs of the modal parameters and the corresponding posterior c.o.v. are shown in Table 15. The natural frequencies of the first two modes are around 2.5Hz. The posterior c.o.v. of damping ratio for these two modes are relatively high compared to those of other modes.

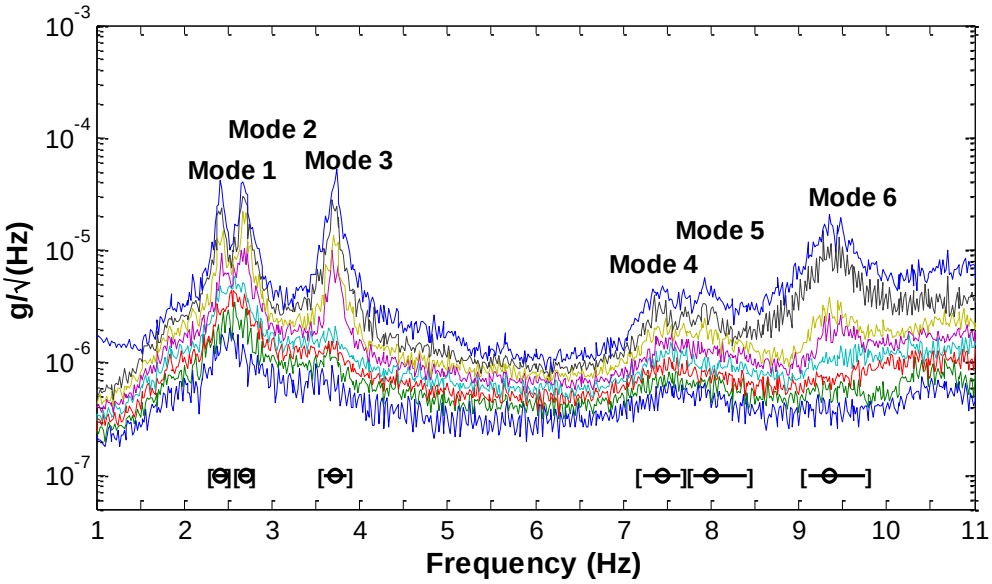

Figure 5. Root Singular Value Spectrum, Brodie Tower Building

Table 15. Identified Modal Parameters, Brodie Tower

Mode	$f\,(Hz)$		$\zeta(\%)$		$\sqrt{S}\,(\mu g/\sqrt{Hz})$		$\sqrt{S_{ej}}\,(\mu g/\sqrt{Hz})$	
	MPV	c.o.v.(%)	MPV	c.o.v.(%)	MPV	c.o.v.(%)	MPV	c.o.v.(%)
1	2.418	0.07	1.32	8.4	1.28	5.4	3.01	4.2
							3.34	4.2
							2.85	4.2
							2.94	4.2
2	2.678	0.06	1.08	8.5	1.32	5.4	3.40	4.3

							3.64	4.3
							3.95	4.3
							1.52	4.3
3	3.714	0.04	0.90	5.0	1.05	2.5	1.24	2.9
							1.26	2.9
							1.34	2.9
							1.99	2.9
4	7.420	0.08	2.21	7.3	0.24	5.6	0.79	2.2
							1.28	2.2
							1.10	2.2
							1.16	2.2
5	7.932	0.12	2.41	5.8	0.26	4.5	1.40	1.7
							0.74	1.7
							0.92	1.7
							1.09	1.7
6	9.391	0.05	1.97	3.8	0.77	2.6	0.79	1.8
							0.76	1.8
							0.73	1.8
							1.39	1.8

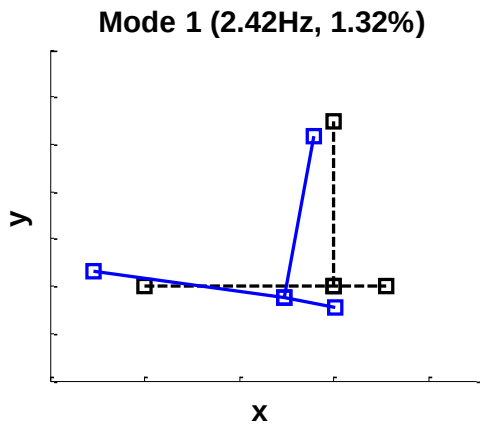

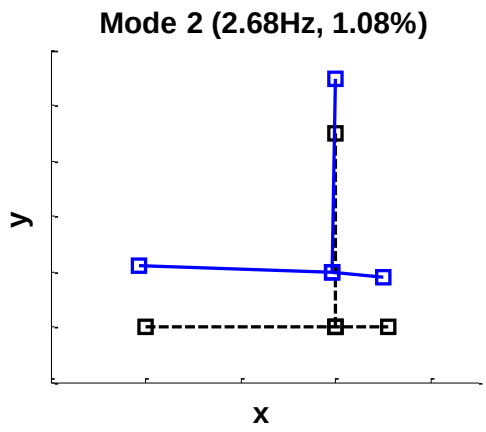

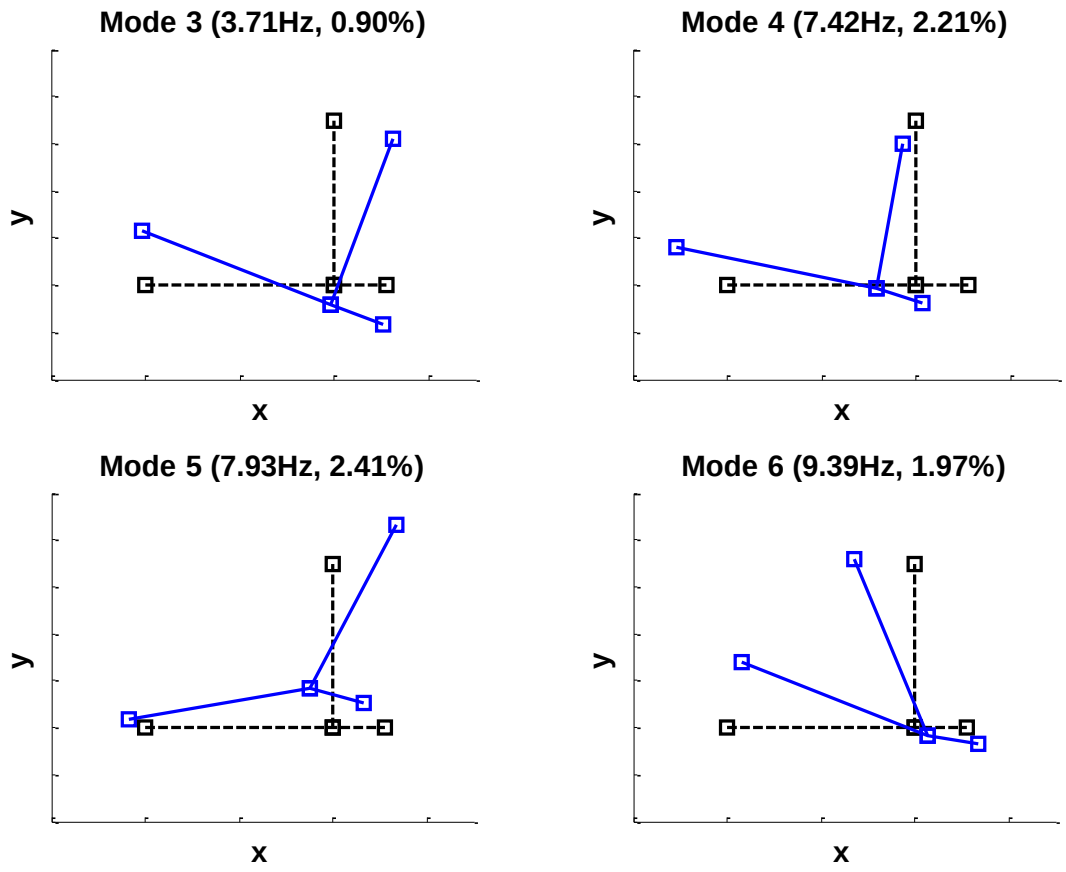

Figure 6. Identified Mode Shapes (MPV), Brodie Tower Asynchronous Data

Figure 6 shows the identified mode shapes (MPV) of these five modes in plan view. The dashed line and solid line denote the undeformed and deformed mode shapes, respectively. The squares represent the measured locations. Mode 1 and Mode 4 are primarily translational in the x-direction. A small rotation can be found in these two modes, which may be due to the shape of the floor and distribution of mass, etc. Mode 2 is translational in the y-direction. Mode 3 is rotational. Mode 5 and Mode 6 involve deformation of the T-shaped floor plan.

Additional data have been analysed with the same test configurations while in this case the sensors were synchronised using GPS (Global Positioning System). Figure 7 summarises the identification results. It can be seen that the identified natural frequencies and damping ratios based on the asynchronous data are close to those based on the synchronous data. Small discrepancies can be found, which are mainly due to the variation of the environmental conditions. The identified mode shapes based on the asynchronous data almost coincide with those based on the synchronous data. The MAC values are calculated to be 0.9997, 0.9995, 0.9994, 0.9749, 0.9794 and 0.9287 from Mode 1 to Mode 6 respectively, suggesting good identification quality using the proposed method for asynchronous data.

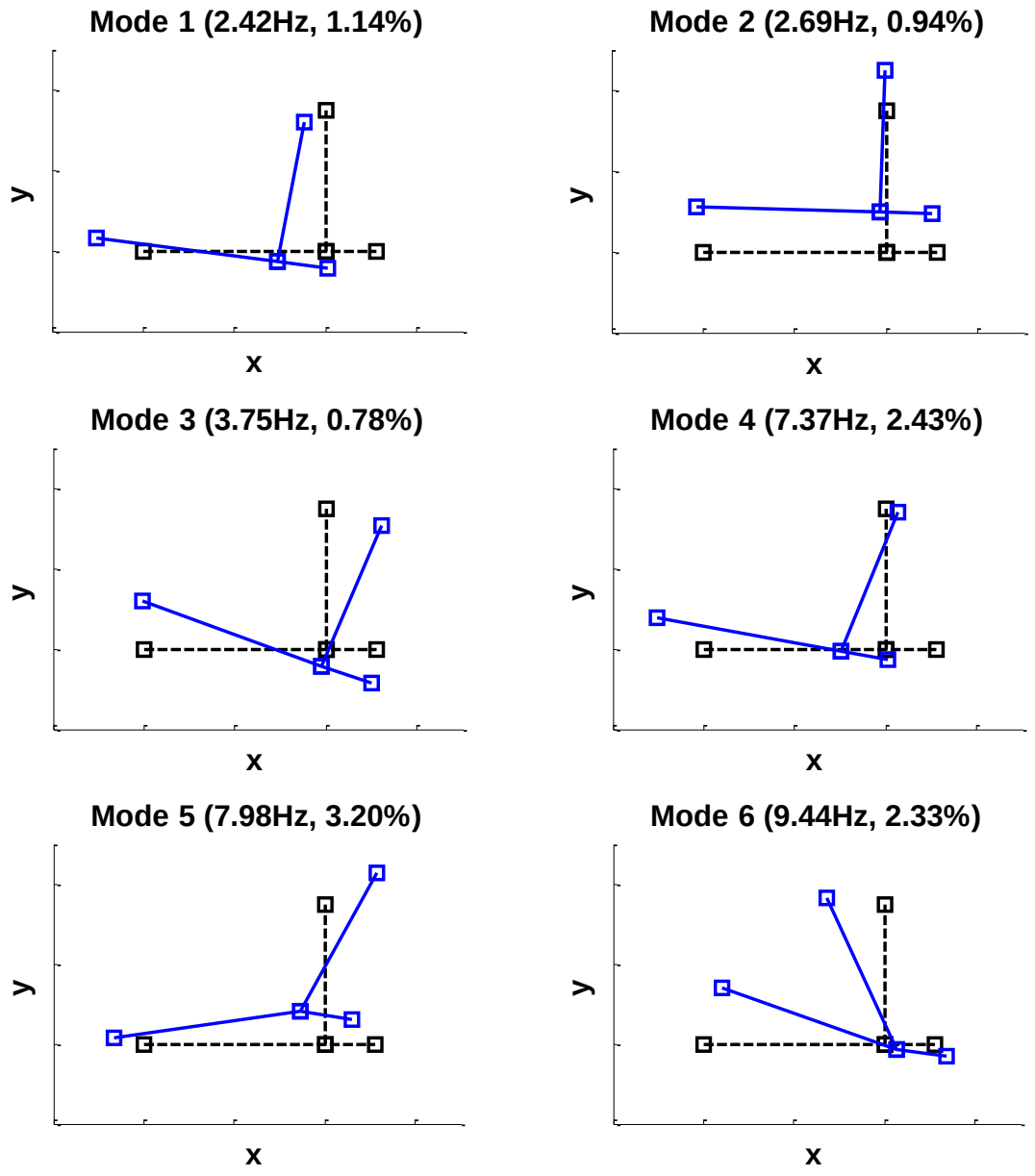

Figure 7. Identified Mode Shapes (MPV), Brodie Tower Synchronous Data

Conventionally, it takes around 20 to 30mins for each accelerometer used in this test to be fully synchronised with each other based on a common external clock source. Without the time synchronisation issue, the configuration time can be significantly reduced and the field test can be more flexibly conducted based on the proposed method.

5. Computational Time

The computational time for determining the MPVs and the posterior uncertainty using the proposed method is discussed in this section. The calculations were performed using

MATLAB R2014a on an HP Compaq 800 G1 Elite Desktop (Intel Core i5, 2GHz and 8GM of RAM). The convergence tolerance in the iteration is set to be 10^{-6} on a fractional basis for all parameters. The computational time and the number of iterations required for determining the MPVs in the examples are shown in Table 16. For the synthetic and laboratory examples, the MPVs can be determined in a few seconds. In the field test example, it takes a few tens of seconds to determine the MPVs for Mode 4 to Mode 6, which may be due to the lower s/n ratio comparing to other modes. The time needed for calculating the posterior uncertainty using the proposed method and finite difference method is shown in Table 17. The finite difference method took much longer time than the proposed method (generally more than 10 times). Note that the accuracy of finite difference method depends on the step length used. To get accurate evaluation results, convergence test is needed, implying additional analysis overhead. In general, the total computation time to determine the MPV and posterior c.o.v. using the proposed method among the examples in this paper is less that one minute.

Table 16. Computational Time, MPV

Example	Mode	No. of Iteration	Time Required (s)
Synthetic Data	1	9	1.8
	2	8	5.2
	3	12	9.2
	4	31	19
Laboratory Shear Building	1	72	1.8
	2	45	4.1
	3	39	3.8
	4	27	5.0
	5	62	0.3
Brodie Tower	1	26	3.4
	2	27	3.2
	3	13	3.4
	4	62	27
	5	52	32
	6	39	28

Table 17. Computational Time, Posterior c.o.v.

Example	Mode	Proposed Method (s)	Finite Difference (s)
Synthetic Data	1	0.68	10.6
	2	1.60	35.3
	3	1.95	42.4
	4	1.61	35.5
Laboratory Shear Building	1	0.26	0.52
	2	0.41	2.37
	3	0.41	2.37
	4	0.62	4.66
	5	0.43	4.67
Brodie Tower	1	0.50	10.5
	2	0.24	9.6
	3	0.55	21.5
	4	0.95	36.8
	5	1.47	52.9
	6	1.45	55.7

6. Discussion

Some final comments are in order regarding the practical issues when applying the proposed method:

1. Although it may be a rare situation in practice, the mode shape values will be small when all the measured DOFs are nodes in one synchronous data group. In this case the quality of the identification results associated with the ith group will clearly be affected (poor), as will the results of any identification method because there is not enough information from data. However, this issue will not cause any legitimacy problem in the proposed theory, i.e., the algorithm can still be applied.
2. A set of data channels is considered as one synchronous group if they are sampled based on the same clock. The total number of synchronous groups is equal to the number of sampling clocks involved in the test. It will be equal to the number of DAQ (data acquisition) units if each DAQ unit uses its own internal clock for sampling. In applications, some DAQ units can be synchronised using a common external clock

like Network Time Protocol or Global Positioning System. In this context, the channels of data measured by these DAQ units are considered as one synchronous group.

3. The practical way to assess the time synchronisation problem is to investigate the measured data directly. Simply looking at the technical specifications on the time drifts of the sampling clocks may not be relevant as the coherence value between synchronous groups varies with the data duration as well as the frequency band of interest. Looking at the technical specifications of the sampling clocks can give a rough idea but the most direct way is to look at the singular value spectrum of data directly. When additional peaks exhibiting almost the same frequency and damping are found in the singular value spectrum and there is no reason to believe the existence of such closely-spaced modes, time synchronisation issues should be investigated and taken into consideration when the data is confirmed to be asynchronous.
4. The Bayesian OMA approach developed in this paper looks similar to the one for multiple-setup tests previously proposed by the second author [17]. However, these two methods are in fact quite different and the latter cannot be directly applied to asynchronous data, or vice versa. The model assumptions between these two cases are different. For asynchronous data, the measured data in different synchronous groups share the same modal properties (i.e., natural frequencies, damping ratios and modal force PSDs) because they are measured during the same time period. For multi-setups, modal properties among different setups are parameterised separately because they can possibly differ due to the variation of environmental conditions. In the asynchronous data problem, the relative scaling between the partial mode shapes in different synchronous groups are determined based on the same modal force PSD. In the multi-setup data problem, the relative scaling among the mode shapes in different setups are determined based on the mode shape values at the reference DOFs.

7. Conclusions

In this work, a Bayesian formulation for modal identification using asynchronous ambient vibration data has been developed. An efficient iterative algorithm for determining the MPVs has been proposed in the companion paper. Efficient strategies have been developed for calculating the posterior covariance matrix without resorting to finite difference method.

The proposed algorithms assume zero coherence among the synchronous data groups. Potential modelling error due to this approximation has been investigated through a parametric study. The results reveal that the bias in the MPV is not significant. Posterior uncertainty of frequency and damping is biased low, although it is not significant unless the coherence is very high. The proposed method has been tested with synthetic and laboratory data; and applied to field data of a multi-storey building. The MPV and posterior uncertainty can be evaluated in a matter of seconds using the proposed method.

Time synchronisation issue in operational modal analysis is currently a challenging problem and the characteristics of the imperfect coherence due to asynchronisation have not been fully understood yet. It is hoped that this work provides some insights on this problem and inspirations for subsequent investigation.

Acknowledgments

This paper was partly supported by Tung Doctoral Scholarship and UK Engineering & Physical Sciences Research Council (EP/N017897/1). The financial support is gratefully acknowledged.

Appendix: Derivatives of D_k and D_k^{-1}

This appendix presents the derivatives of D_k in Eq.(3). Recalling from [10], they can be expressed in terms of the derivatices of its reciprocal D_k^{-1}. In general, for any two variables x_1 and x_2:

$$D_k^{(x_1)} = -D_k^{\,2}\left(D_k^{-1}\right)^{(x_1)} \tag{38}$$

$$D_k^{(x_1x_2)} = 2D_k^{\,3}\left(D_k^{-1}\right)^{(x_1)}\left(D_k^{-1}\right)^{(x_2)} - D_k^2\left(D_k^{-1}\right)^{(x_1x_2)} \tag{39}$$

The derivatives of D_k^{-1} with respect to f and ζ are given by

$$\left(D_k^{-1}\right)^{(f)} = 4 f_k^{-1}\left[\beta_k^3 - \beta_k\left(1-2\zeta^2\right)\right] \tag{40}$$

$$\left(D_k^{-1}\right)^{(\zeta)} = 8\zeta\beta_k^2 \tag{41}$$

$$\left(D_k^{-1}\right)^{(ff)} = 4 f_k^{-2}\left[3\beta_k^2 - 1 + 2\zeta^2\right] \tag{42}$$

$$\left(D_k^{-1}\right)^{(\zeta\zeta)} = 8\beta_k^2 \tag{43}$$

$$\left(D_k^{-1}\right)^{(f\zeta)} = 16 f_k^{-1}\zeta\beta_k \tag{44}$$

References

[1] C.R. Farrar, K. Worden, An introduction to structural health monitoring., Philos. Trans. A. Math. Phys. Eng. Sci. 365 (2007) 303–315. doi:10.1098/rsta.2006.1928.

[2] F.N. Catbas, T. Kijewski-Correa, A.E. Aktan, Structural identification (St-Id) of constructed facilities: Approaches, methods and technologies for effective practice of St-Id, in: Am Soc Civ Eng, 2011.

[3] E.P. Carden, A. Mita, Challenges in developing confidence intervals on modal parameters estimated for large civil infrastructure with stochastic subspace identification, Struct. Control Heal. Monit. 18 (2009) 53–79. doi:10.1002/stc.358.

[4] R. Pintelon, P. Guillaume, J. Schoukens, Uncertainty calculation in (operational) modal analysis, Mech. Syst. Signal Process. 21 (2007) 2359–2373. doi:10.1016/j.ymssp.2006.11.007.

[5] E. Reynders, R. Pintelon, G. De Roeck, Uncertainty bounds on modal parameters obtained from stochastic subspace identification, Mech. Syst. Signal Process. 22 (2008) 948–969. doi:10.1016/j.ymssp.2007.10.009.

[6] M. Döhler, X.B. Lam, L. Mevel, Uncertainty quantification for modal parameters from stochastic subspace identification on multi-setup measurements, Mech. Syst. Signal Process. 36 (2013) 562–581. doi:10.1016/j.ymssp.2012.11.011.

[7] T.J. Matarazzo, S.N. Pakzad, Sensitivity Metrics for Maximum Likelihood System Identification, ASCE-ASME J. Risk Uncertain. Eng. Syst. Part A Civ. Eng. (2015). doi:10.1061/AJRUA6.0000832.

[8] J.L. Beck, Bayesian system identification based on probability logic, Struct. Control Heal. Monit. 17 (2010) 825–847. doi:10.1002/stc.424.

[9] C. Papadimitriou, J.L. Beck, L.S. Katafygiotis, Updating robust reliability using structural test data, Probabilistic Eng. Mech. 16 (2001) 103–113. doi:10.1016/S0266-

8920(00)00012-6.

[10] S.-K. Au, Fast Bayesian FFT method for ambient modal identification with separated modes, J. Eng. Mech. (2011). doi:10.1061/(ASCE)EM.1943-7889.0000213.

[11] S.-K. Au, Fast Bayesian ambient modal identification in the frequency domain, Part II: Posterior uncertainty, Mech. Syst. Signal Process. 26 (2012) 76–90. doi:10.1016/j.ymssp.2011.06.019.

[12] F.-L. Zhang, S.-K. Au, H.-F. Lam, Assessing uncertainty in operational modal analysis incorporating multiple setups using a Bayesian approach, Struct. Control Heal. Monit. (2014). doi:10.1002/stc.1679.

[13] S.-K. Au, Connecting Bayesian and frequentist quantification of parameter uncertainty in system identification, Mech. Syst. Signal Process. 29 (2012) 328–342. doi:10.1016/j.ymssp.2012.01.010.

[14] S.-K. Au, Uncertainty law in ambient modal identification---Part II: Implication and field verification, Mech. Syst. Signal Process. 48 (2014) 34–48. doi:10.1016/j.ymssp.2013.07.017.

[15] E.M. Hernandez, N.R. Polanco, A lower bound for the variance of frequency and damping ratio identified from noisy vibration measurements, Struct. Control Heal. Monit. 23 (2016) 5–19. doi:10.1002/stc.1757.

[16] S.-K. Au, F.-L. Zhang, On assessing the posterior mode shape uncertainty in ambient modal identification, Probabilistic Eng. Mech. 26 (2011) 427–434. doi:10.1016/j.probengmech.2010.11.009.

[17] S.-K. Au, F.-L. Zhang, Fast Bayesian ambient modal identification incorporating multiple setups, J. Eng. Mech. (2012) 800–815. doi:10.1061/(ASCE)EM.1943-7889.0000385.